

The relation between star formation rate and stellar mass of galaxies at $z \sim 1 - 4$

A. Katsianis^{1,2*}, E. Tescari^{1,2}, and J. S. B. Wyithe^{1,2}

¹School of Physics, The University of Melbourne, Parkville, VIC 3010, Australia

²ARC Centre of Excellence for All-Sky Astrophysics (CAASTRO)

Abstract

The relation between the Star Formation Rate (SFR) and stellar mass (M_*) of galaxies represents a fundamental constraint on galaxy formation, and has been studied extensively both in observations and cosmological hydrodynamic simulations. However, the observed amplitude of the star formation rate - stellar mass relation has not been successfully reproduced in simulations, indicating either that the halo accretion history and baryonic physics are poorly understood or that observations contain biases. In this paper, we examine the evolution of the SFR- M_* relation of $z \sim 1 - 4$ galaxies and display the inconsistency between observed relations that are obtained using different techniques. We employ cosmological hydrodynamic simulations from various groups and compare these with a range of observations. The comparison suggests that using Spectral Energy Distributions (SEDs) to estimate star formation rates, dust corrections and stellar masses produces the most reliable SFR- M_* relations. On the contrary, the combination of IR and UV luminosities (UV+IR) overpredicts the SFR and dust corrections at a fixed stellar mass almost by a factor of 5 for $z \sim 1.5 - 4$. For $z < 1.5$, the SED fitting technique and IR+UV conversion agree well. In addition, surveys that preferably select star forming galaxies (e.g. by adopting Lyman-break selection or $H\alpha$ selection) overpredict the median/average star formation rate at a fixed stellar mass especially for high mass objects. Furthermore, updated observed star formation rate - stellar mass relations that are able to take into account faint small mass objects with low star formation rates tend to be steeper than previous estimates, and in good agreement with predictions from cosmological simulations. We find remarkable agreement between the numerical results from various authors who have employed different cosmological codes and run simulations with different resolutions. This is interesting for two reasons. A) simulations can produce realistic populations of galaxies within representative cosmological volumes even at relatively modest resolutions. B) It is likely that current numerical codes that rely on similar subgrid multiphase ISM models and are tuned to reproduce statistical properties of galaxies, produce similar results for the SFR- M_* relation by construction, regardless of resolution, box size and, to some extent, the adopted feedback prescriptions.

Keywords: cosmology: theory – galaxies: evolution – methods: numerical

1 Introduction

Numerous studies have demonstrated a correlation between galaxy star formation rates and stellar masses at redshifts $z \sim 1 - 4$. These studies have employed various observing strategies to sample the galaxy population as completely as possible (Noeske et al. 2007; Elbaz et al. 2007; Daddi et al. 2007; Drory & Alvarez 2008; Kajisawa et al. 2010; Karim et al. 2011; Bauer et al. 2011; Gilbank et al. 2011; Reddy et al. 2012; Bouwens et al. 2012; Heinis et al. 2014; Koyama et al. 2013; Guo et al. 2013; de Barros et al. 2014; Speagle et al. 2014). Galaxies are usually selected using one of the following four techniques.

1. Lyman-break selection: in the absence of dust extinction, star forming galaxies have a flat continuum at rest

frame ultraviolet wavelengths. However, blueward of the Lyman break (rest-frame 912 Å), photoelectric absorption by galactic or extragalactic sources of neutral hydrogen sharply cuts the emitted spectrum. High redshift sources can be selected using this spectral break. This method has been extensively used to construct samples of galaxies at different epochs and study their Star Formation Rate-Stellar Mass (SFR- M_*) relation (Reddy et al. 2012; Bouwens et al. 2012; Heinis et al. 2014; de Barros et al. 2014). An important drawback of this technique is that it is only capable of selecting objects with young ages, high star formation rates and low dust content. Only these galaxies are able to produce a large amount of UV light which is not absorbed by dust. This makes the Lyman-break technique insensitive to galaxies that are dust-reddened or contain evolved stellar populations.

*kata@student.unimelb.edu.au

2. $H\alpha$ selection: in this case, galaxies are selected by their emission in the $H\alpha$ line (rest-frame 6563), which is correlated with star formation and has the advantage that it is not substantially affected by dust attenuation (unlike UV-optical colors). Various authors have constructed $H\alpha$ selected samples to study the evolution of the cosmic star formation rate density and SFR– M_\star relation (e.g. Sobral et al. 2013; Koyama et al. 2013).
3. SFR selection: a color cut is applied to the parent sample of galaxies, so that only blue star forming objects can be included (Noeske et al. 2007; Elbaz et al. 2007; Daddi et al. 2007; Gilbank et al. 2011; Guo et al. 2013). This selection is used to reject possible contaminations from emission line objects whose emission is not due to star-formation. SFR selection includes actively star-forming galaxies. Passive or highly star forming systems with large contents of dust are excluded from this technique.
4. Mass selection: the K-band luminosity of galaxies measures mass in old stars and so is a robust estimator of galaxy stellar mass (Broadhurst et al. 1992; Brinchmann & Ellis 2000). In this case, galaxies are selected by their luminosity in this band and then the redshift is estimated using Spectral Energy Distribution (SED) fitting (Drory & Alvarez 2008; Kajisawa et al. 2010; Karim et al. 2011; Bauer et al. 2011). In contrast to the other selection methods discussed above, stellar mass selection includes galaxies with high contents of dust and/or high stellar masses. However, the K-band magnitude limit of surveys can restrict the stellar mass distribution at the low mass end. This is one of the drawbacks of a magnitude-limited survey (Reddy et al. 2012). Drory et al. (2005) showed that galaxies can also be selected by mass using I-band, yielding mass functions that are consistent with K-band selection.

A comparison between results obtained by using different selection criteria suggests that the observed SFR– M_\star relation is subjected to selection effects and biases (Speagle et al. 2014; Katsianis et al. 2015). In addition to selection effects that can introduce a significant discrepancy between different groups, various authors use different methods to obtain the intrinsic SFRs and dust corrections of the observed galaxies (Kajisawa et al. 2010; Bauer et al. 2011). The most common techniques are:

- 1) Conversion of IR+UV luminosities to SFRs;
- 2) SED fitting (e.g. Bruzual & Charlot 2003) to obtain dust corrections and/or SFRs.

Interestingly, Kajisawa et al. (2010) and Bauer et al. (2011) demonstrated that the above different techniques produce different SFR– M_\star relations for the same sample of galaxies at high redshifts. When the authors used the conversion of IR and UV luminosities, instead of SED fitting,

to estimate dust corrections, they obtained higher values of SFR at a fixed stellar mass. Furthermore, Utomo et al. (2014) claimed that the cosmic star formation rate density inferred by converting UV and IR luminosities is overestimated relative to the one obtained by detailed modeling. Boquien et al. (2014) also argued that SFRs obtained from a synthetic model that takes into account only FUV and U bands are overestimated. Despite the fact that SED fitting techniques imply SFR– M_\star relations that are inconsistent with results that rely on IR+UV-SFR conversions, it is quite common for compilation studies to combine SFR(M_\star) that were obtained employing different methods (Behroozi et al. 2013; Speagle et al. 2014). In Table 1 we present a summary of the different observations used for this work. We include the technique, sample selection, mass limit and area of sky covered.

Motivated by its importance in understanding galaxy evolution, a number of authors (e.g. Davé 2008; Dutton et al. 2010; Finlator et al. 2011; Dayal & Ferrara 2012; Kannan et al. 2014; Sparre et al. 2015; Furlong et al. 2015; Katsianis et al. 2015) have used hydrodynamic and semi-analytic models to predict the SFR– M_\star relation and its evolution. Numerical results (e.g. Davé 2008) predict a steeper relation than is found in observations. For example, the SFR– M_\star relation presented by Kannan et al. (2014) provides good agreement with the observed relation of Kajisawa et al. (2010) for $z \sim 3$. On the other hand, for redshift $z \sim 2.2$ the simulated galaxies have a star formation rate that is only half as large as observed. Katsianis et al. (2015) reported a discrepancy between the simulated SFR– M_\star relation and the observed relations of Bouwens et al. (2012) and Heinis et al. (2014) at $z \sim 4$. Good agreement was found between numerical results and the observations of Drory & Alvarez (2008) and de Barros et al. (2014). More recently, Sparre et al. (2015) used high resolution simulations to investigate the SFR– M_\star relation for redshifts $z \sim 0 - 4$ as part of the Illustris project (Genel et al. 2014). At $z \sim 4$ and $z \sim 0$, the authors are in good agreement with the observed relation of Behroozi et al. (2013). However, the normalisation of the simulated relation is significantly lower than the observational constraints at $z \sim 1$ and $z \sim 2$. In addition, the simulated relation is steeper than observed at all redshifts. In another study, Furlong et al. (2015) showed agreement between simulated and observed specific SFR (sSFR \equiv SFR/ M_\star) - stellar mass relations at $z \sim 0$ using high resolution simulations from the EAGLE project (Schaye et al. 2015). However, once again, the observed relations have a significantly higher normalization at $z \sim 1$ and $z \sim 2$. The tension between observations and simulations, especially at intermediate redshifts, implies either that the current models of galaxy evolution are incomplete or that observations are being misinterpreted.

This paper is the third of a series, in which we seek to study a range of models for galaxy formation in hydrodynamical simulations through comparisons with observations of SFR and stellar mass across cosmic time. In the first paper (Tescari et al. 2014) we constrained and compared our hydrodynamic simulations with observations of

the cosmic star formation rate density and Star Formation Rate Function (SFRF). In the second paper (Katsianis et al. 2015) we demonstrated that the same cosmological hydrodynamic simulations reproduce the observed Galaxy Stellar Mass Function (GSMF) and SFR– M_\star relation for the same redshift interval. In this work, we extend the analysis presented in Katsianis et al. (2015) down to $z \sim 1$, and critically address the comparison of SFR– M_\star relations with observations using different analysis techniques. In section 2 we briefly summarize our numerical methodology. In section 3 we compare our results with the simulated SFR– M_\star relations from different groups and demonstrate the excellent consistency between numerical results from various projects (e.g. ANGUS, Illustris, EAGLE). In section 4 we present the evolution of the SFR– M_\star relation alongside observations from different groups. We draw our conclusions in section 5. In Appendix A we discuss how the uncertainty of the observed SFR– M_\star relation has affected the comparison with simulations in the past.

2 Simulations

In this work we use the set of *AustraliaN GADGET-3 early Universe Simulations* (ANGUS) described in Tescari et al. (2014)¹. We run these simulations using the hydrodynamic code P-GADGET3(XXL). We assume a flat Λ cold dark matter (Λ CDM) model with $\Omega_{\text{om}} = 0.272$, $\Omega_{\text{ob}} = 0.0456$, $\Omega_\Lambda = 0.728$, $n_s = 0.963$, $H_0 = 70.4 \text{ km s}^{-1} \text{ Mpc}^{-1}$ (i.e. $h = 0.704$) and $\sigma_8 = 0.809$. Our configurations have box size $L = 24 \text{ Mpc}/h$, initial mass of the gas particles $M_{\text{GAS}} = 7.32 \times 10^6 M_\odot/h$ and a total number of particles equal to 2×288^3 . All the simulations start at $z = 60$ and were stopped at $z = 0.8$. For this work we use a Chabrier (2003) Initial Mass Function (IMF) for all configurations.

We explore different feedback prescriptions, in order to understand the origin of the difference between observed and simulated relationships. We also study the effects of metal cooling. We do not explore the broadest possible range of simulations, but concentrate on the simulations that can describe the high- z star formation rate function and galaxy stellar mass function. We performed resolution tests for high redshifts ($z \sim 4 - 7$) in the appendix of (Katsianis et al. 2015) and showed that our results converge for objects with $\log_{10}(M_\star/M_\odot) \geq 8.5$. In Table 2 we summarise the main parameters of the cosmological simulations performed for this work.

2.1 SNe feedback

We investigate the effect of three different galactic winds schemes in the simulated SFR– M_\star relation. For the case of supernova driven winds, we use the implementation of

galactic winds of Springel & Hernquist (2003). We assume the wind mass loading factor $\eta = \dot{M}_w/\dot{M}_\star = 2$ and a fixed wind velocity $v_w = 450 \text{ km/s}$. In addition, we explore the effects of variable winds. We use a momentum driven wind model in which the velocity of the winds is proportional to the circular velocity v_{circ} of the galaxy:

$$v_w = 2 \sqrt{\frac{GM_{\text{halo}}}{R_{200}}} = 2 \times v_{\text{circ}}, \quad (1)$$

and the loading factor η ,

$$\eta = 2 \times \frac{450 \text{ km/s}}{v_w}, \quad (2)$$

where M_{halo} is the halo mass and R_{200} is the radius within which a density 200 times the mean density of the Universe at redshift z is enclosed (Barai et al. 2013). Furthermore, we investigate the effect of the energy driven winds used by Puchwein & Springel (2013). In this case the loading factor is

$$\eta = 2 \times \left(\frac{450 \text{ km/s}}{v_w} \right)^2, \quad (3)$$

while $v_w = 2 \times v_{\text{circ}}$.

2.2 AGN feedback

In our scheme for Active Galactic Nuclei (AGN) feedback, when a dark matter halo reaches a mass above a given mass threshold $M_{\text{th}} = 2.9 \times 10^{10} M_\odot/h$ for the first time, it is seeded with a central Super-Massive Black Hole (SMBH) of mass $M_{\text{seed}} = 5.8 \times 10^4 M_\odot/h$ (provided it contains a minimum mass fraction in stars $f_\star = 2.0 \times 10^{-4}$). Each SMBH will then increase its mass by accreting local gas from a maximum accretion radius $R_{\text{ac}} = 200 \text{ kpc}/h$. In this scheme we allow the presence of a black hole in low mass halos, and at early times. The AGN feedback prescription that we use combined with efficient winds is successful at reproducing the observed SFRF (Tescari et al. 2014) and GSMF (Katsianis et al. 2015) for redshifts $4 < z < 7$.

2.3 Metal cooling

Our code follows the evolution of 11 elements (H, He, C, Ca, O, Ne, Mg, S, Si and Fe) released from supernovae (SNIa and SNI) and low and intermediate mass stars self-consistently (Tornatore et al. 2007). Radiative heating and cooling processes are included following Wiersma et al. (2009). We assume a mean background radiation composed of the cosmic microwave background and the Haardt & Madau (2001) ultraviolet/X-ray background from quasars and galaxies. Contributions to cooling from each one of the eleven elements mentioned above have been pre-computed using the Cloudy photo-ionisation code (last described in Ferland et al. 2013) for an optically thin gas in (photo)ionisation equilibrium. In this work we use cooling tables for gas of

¹The features of our code are extensively described in Tescari et al. (2014) and Katsianis et al. (2015), therefore we refer the reader to those papers for additional information.

Table 1 Summary of the different observations used for this work.

Publication	Redshift	Technique for dust corrections	Sample selection	Mass limit [M _⊙]	Area [deg ²]	Original IMF
Noeske et al. (2007)	0.8, 1.0	EL/IR	SFR	10 ^{10.0}	0.5	Kroupa (2001)
Elbaz et al. (2007)	1.0	UV+IR	SFR	10 ^{8.8} , 10 ^{9.3}	705	Kroupa (2001)
Daddi et al. (2007) ¹	2.0	UV+IR	SFR	10 ^{9.5}	< 0.025	Salpeter (1955)
Drory & Alvarez (2008)	2.2-3.8	SED	Mass	10 ^{9.0}	0.025	Salpeter (1955)
Magdis et al. (2010)	3.0	UV+IR	LBG	10 ^{9.7}	0.296	Salpeter (1955)
Kajisawa et al. (2010)	0.75-3.0	SED	Mass	10 ^{9.5}	0.029	Salpeter (1955)
Kajisawa et al. (2010) ²	0.75-3.0	IR+UV	Mass	10 ^{9.5}	0.029	Salpeter (1955)
Karim et al. (2011)	0.8-3	Radio	Mass/SFR	10 ^{10.1-11.1}	2.0	Chabrier (2003)
Bauer et al. (2011)	1.75-2.75	SED	Mass	10 ^{9.5}	0.13	Salpeter (1955)
Bauer et al. (2011) ²	1.75-2.75	IR+UV	24 μm detected	10 ¹⁰	0.13	Salpeter (1955)
Reddy et al. (2012)	2.0	UV+IR	LBG+Malmquist	10 ^{9.25}	0.44	Salpeter (1955)
Reddy et al. (2012) ³	2.0	UV+IR	LBG, no bias	10 ^{9.25}	0.44	Salpeter (1955)
Bouwens et al. (2012)	3.8	UV corr	LBG	10 ^{7.8}	0.040	Salpeter (1955)
Kashino et al. (2013)	1.5	Hα+UV	Hα	10 ^{10.0}	2.0	Salpeter (1955)
Behroozi et al. (2013)	0-4	Comp	Comp	10 ^{9.0}	Comp	Chabrier (2003)
Bauer et al. (2013)	Local	Hα	Hα	10 ^{9.0}	144	Chabrier (2003)
Koyama et al. (2013)	0.8, 2.2	Hα	Hα	10 ^{9.75}	2.0	Salpeter (1955)
Guo et al. (2013)	0.7	UV+IR	SFR	10 ^{9.5}	1.45	Chabrier (2003)
Heinis et al. (2014)	1.5, 3.0, 4.0	UV+IR	LBG	10 ^{9.5-10.6}	2.0	Chabrier (2003)
De Los Reyes et al. (2014)	0.8	SED	Hα	10 ^{9.27}	0.82	Chabrier (2003)
de Barros et al. (2014)	3.0, 4.0	SED	LBG	10 ^{9.0}	0.044	Salpeter (1955)
Salmon et al. (2015)	4.0	SED	SED	10 ^{9.0}	0.047	Salpeter (1955)

Notes: Column 1, publication reference of the observed SFR–M_★ relation; column 2, redshift used; column 3, technique and type of luminosity used to obtain the intrinsic SFR. These are: Emission lines (EL), Infrared (IR) luminosity, Ultra-Violet (UV) luminosity, Spectral Energy Distribution (SED) and radio luminosity. We include the Compilation (Comp) of studies presented in Behroozi et al. (2013); column 4, sample selection method. These are: Star Formation Rate (SFR), mass, Hα and Lyman Break Galaxy (LBG) selection; column 5, mass limit of the observations; column 6, area covered by the survey in deg²; column 7, original IMF adopted. We present the relations suggested by the authors corrected to a Chabrier (2003) IMF when necessary (this conversion does not affect the relations given since a similar change to SFR and M_★ is used) along with results from cosmological hydrodynamic simulations in Figure 2 ($z \sim 3.1$ and $z \sim 3.8$), Figure 3 ($z \sim 2.2$ and $z \sim 2.6$), Figure 4 ($z \sim 2.0$ and $z \sim 1.5$) and Figure 5 ($z \sim 0.8 - 1.15$). 1) Daddi et al. (2007) used a fraction of the GOODS-N and GOODS-S fields, but did not report an exact area. 2) These observations are for the same sample of galaxies of the original work but adopt different methods for the determination of intrinsic SFRs and dust corrections. 3) This set of observations is corrected for the effects of the Malmquist bias.

primordial composition (H + He) as the reference configuration. To test the effect of metal-line cooling, we include it in two simulations (*Ch24_Zc_eA_EDW* and *Ch24_Zc_eA_CsW*).

3 Comparison between simulated SFR–M_★ relations from different groups

Cosmological hydrodynamic simulations provide a powerful tool to investigate and predict properties of galaxies and their distribution. Recently, the Illustris (Sparre et al. 2015) and EAGLE (Furlong et al. 2015) projects have used high resolution simulations and tried to reproduce the observed SFR–M_★. In addition, semi-analytic models have been used to reproduce the observed relations at various redshifts (Dutton et al. 2010). The two main questions that arise are:

- Are simulations and theory capable of reproducing the observed SFR–M_★ relations?
- Are the results of simulations that are tuned to reproduce certain observables consistent with each other?

In Figure 1 we present a comparison between the simulated median SFR–M_★ relations of our reference model (Project name: ANGUS, black solid line), and those presented in Dutton et al. (2010, blue dotted line, semi-analytic model), Sparre et al. (2015, Illustris, magenta dashed line) and Furlong et al. (2015, EAGLE, red dashed line). For this analysis we do not include galaxies that have masses lower than the confidence limit of 10⁹ M_⊙ from our simulations. This is done to make a meaningful comparison with the Illustris and EAGLE projects. We see the agreement between different groups is excellent despite the fact that they used

Table 2 Summary of the different runs used in this work.

Run	IMF	Box Size [Mpc/h]	N_{TOT}	M_{DM} [M_{\odot}/h]	M_{GAS} [M_{\odot}/h]	Comoving Softening [kpc/h]	Feedback
<i>Ch24_eA_CsW</i>	Chabrier	24	2×288^3	3.64×10^7	7.32×10^6	4.0	Early AGN + Constant strong Winds
<i>Ch24_eA_nW</i>	Chabrier	24	2×288^3	3.64×10^7	7.32×10^6	4.0	Early AGN + no Winds
<i>Ch24_NF</i>	Chabrier	24	2×288^3	3.64×10^7	7.32×10^6	4.0	No Feedback
<i>Ch24_eA_MDW^a</i>	Chabrier	24	2×288^3	3.64×10^7	7.32×10^6	4.0	Early AGN + Momentum-Driven Winds
<i>Ch24_eA_EDW^b</i>	Chabrier	24	2×288^3	3.64×10^7	7.32×10^6	4.0	Early AGN + Energy-Driven Winds
<i>Ch24_Zc_eA_CsW^c</i>	Chabrier	24	2×288^3	3.64×10^7	7.32×10^6	4.0	Early AGN + Constant strong Winds Metal cooling
<i>Ch24_Zc_eA_EDW^c</i>	Chabrier	24	2×288^3	3.64×10^7	7.32×10^6	4.0	Early AGN + Energy-Driven Winds Metal cooling

Notes: Column 1, run name; column 2, Initial Mass Function (IMF) chosen; column 3, box size in comoving Mpc/h; column 4, total number of particles ($N_{\text{TOT}} = N_{\text{GAS}} + N_{\text{DM}}$); column 5, mass of the dark matter particles; column 6, initial mass of the gas particles; column 7, Plummer-equivalent comoving gravitational softening length; column 8, type of feedback implemented. See section 2 and Tescari et al. (2014) for more details on the parameters used for the different feedback recipes. (a): in this simulation we adopt variable momentum-driven galactic winds (Subsection 2.1). (b): in this simulation we adopt variable energy-driven galactic winds (Subsection 2.1). (c): in these simulations the effect of metal-line cooling is included (Subsection 2.3). For all the other runs we use cooling tables for gas of primordial composition (H + He).

Table 3 Summary of the different simulated SFR– M_* relations used for Figure 1.

Publication	redshift	Box Size [Mpc/h]	N_{TOT}	M_{DM} [M_{\odot}/h]	M_{GAS} [M_{\odot}/h]	Comoving Softening [kpc/h]	Feedback
<i>Ch24_eA_EDW</i> (this work)	0, 1.15, 2.0, 3.8	24	2×288^3	3.64×10^7	7.32×10^6	4.0	Early AGN + Energy-Driven Winds
Sparre et al. (2015)	0, 1, 2, 4	75	2×1820^3	4.41×10^6	8.87×10^5	0.704	AGN + Stellar Vogelsberger et al. (2013)
Furlong et al. (2015)	0, 1, 2	70.4	2×1504^3	6.83×10^6	1.27×10^6	1.87	AGN + Stellar Crain et al. (2015)
Dutton et al. (2010) Semi-analytic	0, 1, 2, 4	NA	NA	NA	NA	NA	Stellar Dutton et al. (2010)

Notes: Column 1, publication reference; column 2, redshifts considered; column 3, box size of the simulation in comoving Mpc/h; column 4, number of particles used; column 5, mass of the dark matter particles; column 6, initial mass of the gas particles; column 7, comoving softening length; column 8, feedback prescriptions used. The box size and masses of the dark matter and gas particles are in Mpc/h and M_{\odot}/h , respectively, rescaled to our adopted cosmology ($h = 0.704$).

different resolutions and box sizes (In Table 3 we include some details for the runs that were used to produce the simulated SFR– M_* shown in Figure 1). Models that are tuned to reproduce certain observables (eg. ANGUS - cosmic star formation rate density evolution, EAGLE - GSMF at $z \sim 0$, Dutton et al. (2010) - SFR– M_* relation at $z \sim 0$) produce similar results for the star formation rate main sequence. It is worth to mention that even under our mass confidence mass limit our results are in agreement with Furlong et al. (2015).

Davé (2008) using GADGET-2 (Springel 2005) demonstrated that simulations of galaxy formation produce similar SFR– M_* relations, to a large extent independently of modeling details (e.g feedback prescriptions). According to the authors, this is a generic consequence of smooth and steady cold accretion which dominates the growth of the

simulated objects. In addition, Dutton et al. (2010) state that the SFR– M_* relation is generally found to be independent of feedback, since feedback regulates the outflow rate, and mostly acts to shift galaxies along the SFR sequence, leaving the zero point of the relation invariant. We display the excellent agreement between the SFR– M_* relations found in different cosmological hydrodynamic simulations (ANGUS, Illustris, EAGLE) and the semi-analytic results of Dutton et al. (2010). This strongly suggests that the slope and normalization of the relation have their origins in fundamental principles and assumptions commonly adopted in numerical codes, while the small differences in feedback prescriptions play a negligible role. Our results for the local Universe are consistent with the relations of other groups, despite the fact

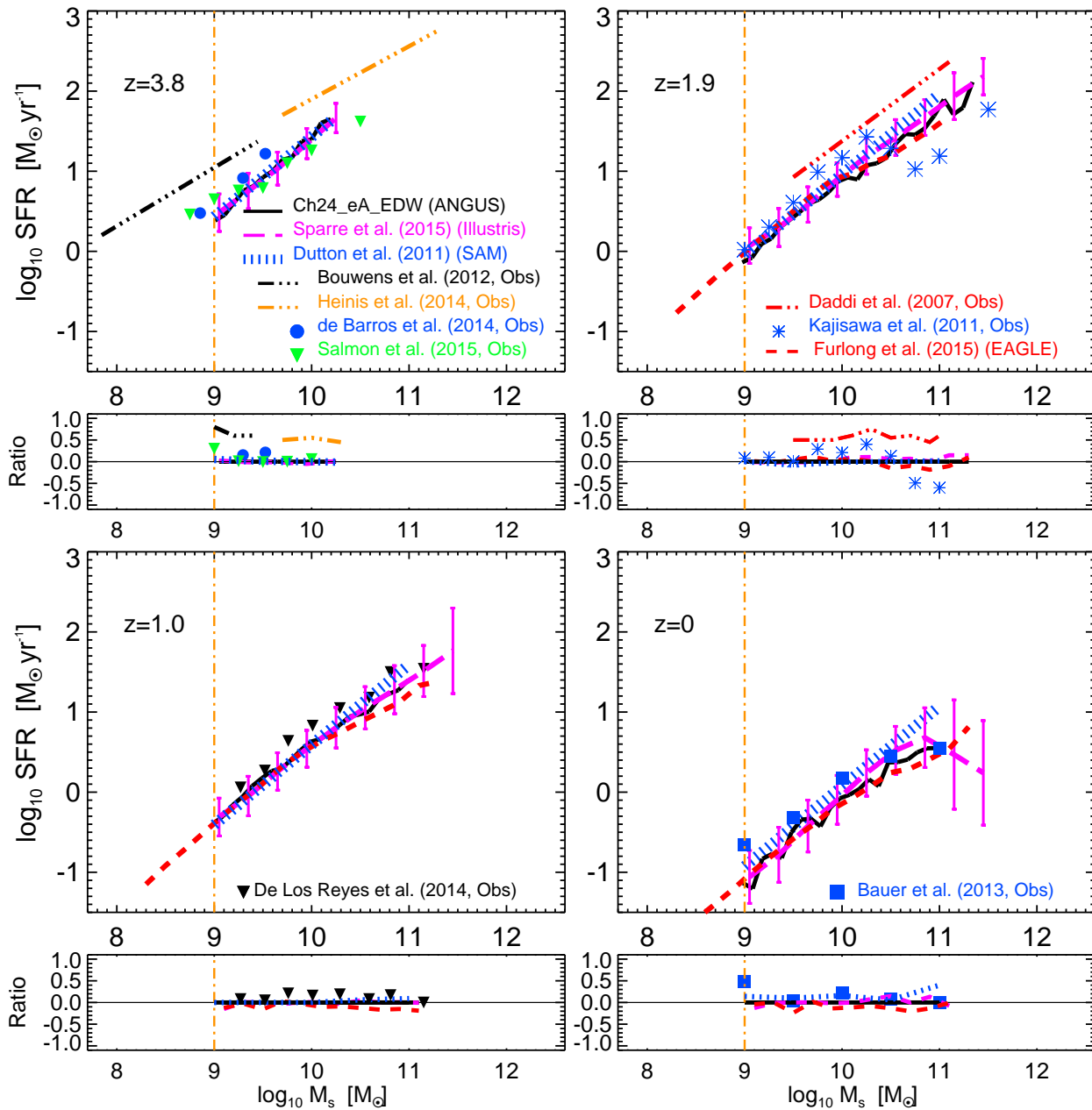


Figure 1. Median values of the SFR– M_{\star} relations from different cosmological hydrodynamic simulations for $z \sim 0 - 4$. The black line is the median line through all the points of the scatter plot for our reference model (*Ch24_eA_EDW*). The blue dotted line is the median fit of the scatter plot obtained with the Semi-Analytic Model (SAM) of Dutton et al. (2010). The magenta dashed line is the median line of the scatter plot presented by Sparre et al. (2015, Illustris project). The red dashed line is the median line of the scatter plot presented by Furlong et al. (2015, EAGLE project). We cut our SFR(M_{\star}) under our confidence mass limit of $10^9 M_{\odot}$ to make a meaningful comparison with the Illustris and EAGLE projects. There is an excellent agreement between the results from cosmological hydrodynamic simulations run by different groups. At each redshift, a panel showing ratios between the different simulations and observations with the *Ch24_eA_EDW* (black solid line) is included.

that our box size and resolution is not sufficient to robustly probe other properties of galaxies at $z \sim 0$.

Increasing the resolution provides a description of smaller masses and scales. In addition, decreasing the softening length will better resolve the feedback mechanisms. For this reason, some authors claim that an exact convergence when resolution is changed is not to be expected (Schaye et al. 2015). However, Murante et al. (2015), who used simu-

lations of disc galaxies (based on the GADGET-3 code), demonstrated that numerical results are remarkably stable against resolution even in runs dedicated to galactic scales. For their ISM multiphase model the authors employed differential equations that describe the evolution of a system composed of cold clouds (where stars form) embedded in hot ambient gas, at unresolved scales (MUPPI). The results from different runs are stable as resolution is decreased even

by a factor of 8. In particular, morphology-related quantities, such as rotation curves and circularity histograms, vary by less than 10 per cent. The SFR varies approximately by the same amount. Murante et al. (2015) suggest that reducing the softening in simulations of disk galaxies by a factor of 6 induces effects related to numerical heating that change their morphologies and central velocities. Doubling the softening parameter results in thicker and less extended discs and increases the bulge mass. However, the results for the integrated properties are not significantly affected. The remarkable agreement between the simulated SFR – M_{\star} relations presented in Figure 1 indicates that cosmological simulations are able to produce realistic populations of galaxies within representative cosmological volumes, even at relatively modest resolutions. Moreover, numerical codes that rely on similar multiphase models and are tuned to reproduce statistical properties of galaxies are “bound” to produce similar results regardless of resolution and box size.

In the following sections we investigate in more detail the redshift evolution of the simulated SFR– M_{\star} relations in the ANGUS project and critically compare the numerical results with observations. It is already visible from Figure 1 that the observed high redshift relations reported by various authors are in tension with each other.

4 Evolution of the SFR– M_{\star} relation from $z \sim 4$ to $z \sim 1$

In Katsianis et al. (2015) we demonstrated that different observations of the SFR– M_{\star} relation are in tension for $z \sim 4 - 7$. This discrepancy was attributed to the different selection methods and techniques for the determination of the intrinsic SFRs and dust corrections of the observed galaxies. In this section we extend that work to $z \sim 1 - 4$, in order to investigate if observations in this redshift interval are also in tension, and address in more detail how sample selection and methodology can affect the comparison with cosmological simulations. We present the SFR– M_{\star} relation obtained from our hydrodynamic simulations along with observations from different groups in Figs. 2 ($z \sim 3.1 - 3.8$), 3 ($z \sim 2.2 - 2.6$), 4 ($z \sim 1.5 - 2.0$) and 5 ($z \sim 0.8 - 1.15$). In the left panels of each figure we show the scatter plots of the SFR– M_{\star} relation for our reference model *Ch24_eA_EDW* (grey points). The black line is the median line through all points of the scatter plot. Our reference model, which combines a Chabrier IMF, early AGN feedback and variable energy driven winds, is able to reproduce the observed galaxy stellar mass function, star formation rate function and cosmic star formation rate density for $z \sim 1 - 7$ galaxies (Tescari et al. 2014; Katsianis et al. 2015). In the right panels we compare the median lines of the scatter plots for all the runs presented in Table 2. The orange vertical line at $10^9 M_{\odot}$ is the confidence limit of our simulations and the mass limit of most observations for the redshifts considered in this work.

The scatter plot of the simulated SFR– M_{\star} for our reference model at $z \sim 3.8$ (top left panel of Figure 2) is consistent with the results of the mass-selected sample of Drory & Alvarez (2008), the Lyman-Break selected sample of de Barros et al. (2014) and the results of Salmon et al. (2015). On the contrary, the SFR– M_{\star} relations obtained by Bouwens et al. (2012) and Heinis et al. (2014), who used the Lyman-Break technique, imply $\sim 3-5$ times more SFR at a fixed stellar mass. All the above authors use various methods to obtain the intrinsic SFRs and dust attenuation effects. Drory & Alvarez (2008) and de Barros et al. (2014) used the SED fitting technique. Whereas, Bouwens et al. (2012) and Heinis et al. (2014) estimated the dust attenuation effects and SFRs in their sample using the IRX– β relation (Meurer et al. 1999), stacking techniques and the Kennicutt (1998) relation. The tension between the above results may be due to the fact that the authors used different methods to obtain the intrinsic properties of galaxies. For redshift $z = 3.8$, our configurations that combine different feedback schemes are not distinct (top right panel of Figure 2). This follows the results of Katsianis et al. (2015), who showed that different feedback prescriptions result in roughly the same SFR– M_{\star} relation for $z \sim 4 - 7$.

At $z \sim 3.1$, our reference model (*Ch24_eA_EDW*, bottom left panel of Figure 2) is consistent with the mass selected observations of Drory & Alvarez (2008) and Kajisawa et al. (2010), and the Lyman-break selected sample of de Barros et al. (2014). Kajisawa et al. (2010) used two different methods to obtain the intrinsic SFRs at a fixed stellar mass for the same sample of galaxies. In the first case, they used the sum of IR and UV light to estimate the observed SFRs for objects that were detected having an IR $24 \mu\text{m}$ flux (originating from dusty high star forming galaxies). For the other objects (undetected at $24 \mu\text{m}$) the authors used SED fitting techniques and UV luminosities. The dark green stars of figure 2 are obtained with this methodology. In the second case, SED fitting technique and UV luminosities were used for the whole sample of galaxies. They find good agreement between both methods at $z \sim 3.0$, even though the SFRs from the combination of UV and IR light are slightly higher than those found by SED fitting. Kajisawa et al. (2010) stressed that, at $z \sim 3$, the ratio $\log(SFR_{IR+UV}/SFR_{UV_{SED}})$ for galaxies with $24 \mu\text{m}$ flux is as high as ~ 0.63 . This is an example of how methodology can affect the determination of SFRs. The relations given by the Lyman-break selection of Magdis et al. (2010) and Heinis et al. (2014) have significantly higher normalizations. The intrinsic SFRs and dust corrections of Heinis et al. (2014) may be overestimated due to the method used (SFR_{UV+IR}). Another possible reason why Heinis et al. (2014) overpredict the SFR at a fixed stellar mass could be their selection method. Heinis et al. (2014) discussed the impact of the Lyman-break selection on their retrieved SFR– M_{\star} relation, and state that their sample may not include a significant number of objects since they preferably select star forming objects. They note that their shallow slope, ~ 0.7 , might be caused by the fact that they are

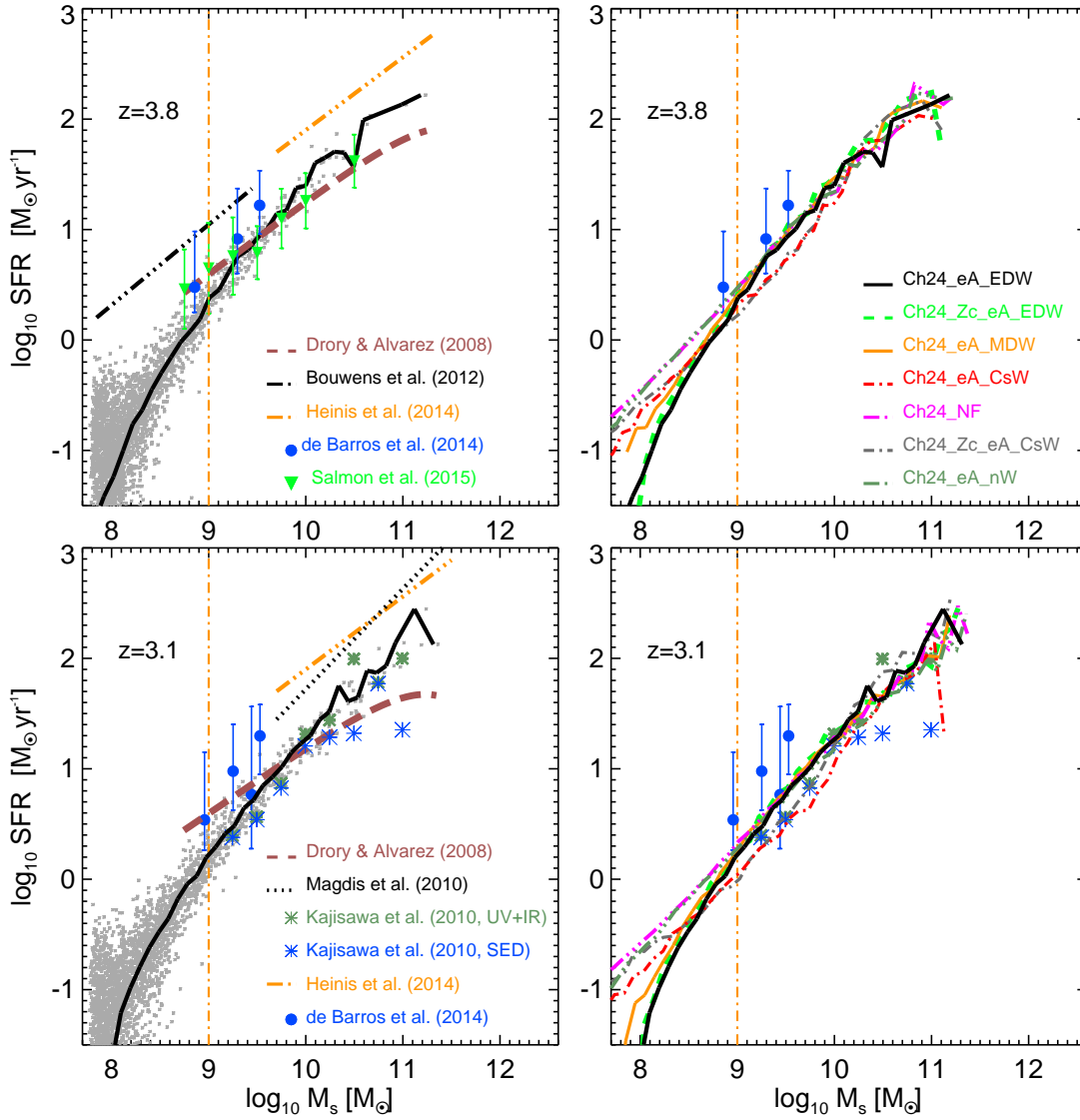


Figure 2. Left panels: scatter plot of the SFR– M_* relation for our fiducial run *Ch24_eA_EDW* (grey points) at redshifts $z \sim 3.1$ and 3.8 . In each panel, the black solid line is the median line through the points of the scatter plot. Overplotted are the observed galaxy SFR(M_*) relations from Drory & Alvarez (2008, mass selected sample - brown dashed line), Magdis et al. (2010, Lyman-break selected sample - black dotted line), Kajisawa et al. (2010, mass-selected sample - the dark green stars represent SFRs that were obtained using UV+IR luminosities, while the blue stars were obtained using the SED fitting technique), Bouwens et al. (2012, Lyman-break selected sample - black triple dot-dashed line), Heinis et al. (2014, Lyman-break selected sample - orange triple dot-dashed line), de Barros et al. (2014, Lyman-break selected sample - blue filled circles with error bars) and Salmon et al. (2015, SED derived redshifts - reverse green triangles with error bars). Right panels: median lines of the SFR– M_* scatter plots for all the runs of Table 2. In these panels we do not present the analytic expressions of the observed relations for the sake of clarity.

selecting galaxies by their UV flux, which does not pick objects with low star formation rates at fixed stellar mass or dusty massive objects. Our simulations produce SFR– M_* relations that are in excellent agreement with mass selected surveys and suggest that the majority of Lyman-break surveys produce shallower relations with higher normalizations (i.e. Lyman-break selection misses a significant number of galaxies).

We see the effect of metal cooling and different feedback prescriptions among the different simulations at $z \sim 3.1$ in the bottom right panel of Figure 2. The *Ch24_NF*

(no feedback) and *Ch24_eA_nW* (early AGN, no winds) runs are almost identical. This means that the effect of our AGN feedback model on the simulated SFR– M_* relation is small. Furthermore, we can compare the *Ch24_eA_nW* and *Ch24_eA_CsW* (early AGN, constant strong winds) to gain insight into how the constant energy wind model of Springel & Hernquist (2003) affects the simulated relation. We see that the star formation rate at fixed mass for objects with stellar mass $\log_{10}(M_*/M_\odot) \leq 10.0$ is lower for the *Ch24_eA_CsW* run. Above the mass limit of $10^9 M_\odot$, the *Ch24_eA_MDW* (early AGN, momentum-driven winds)

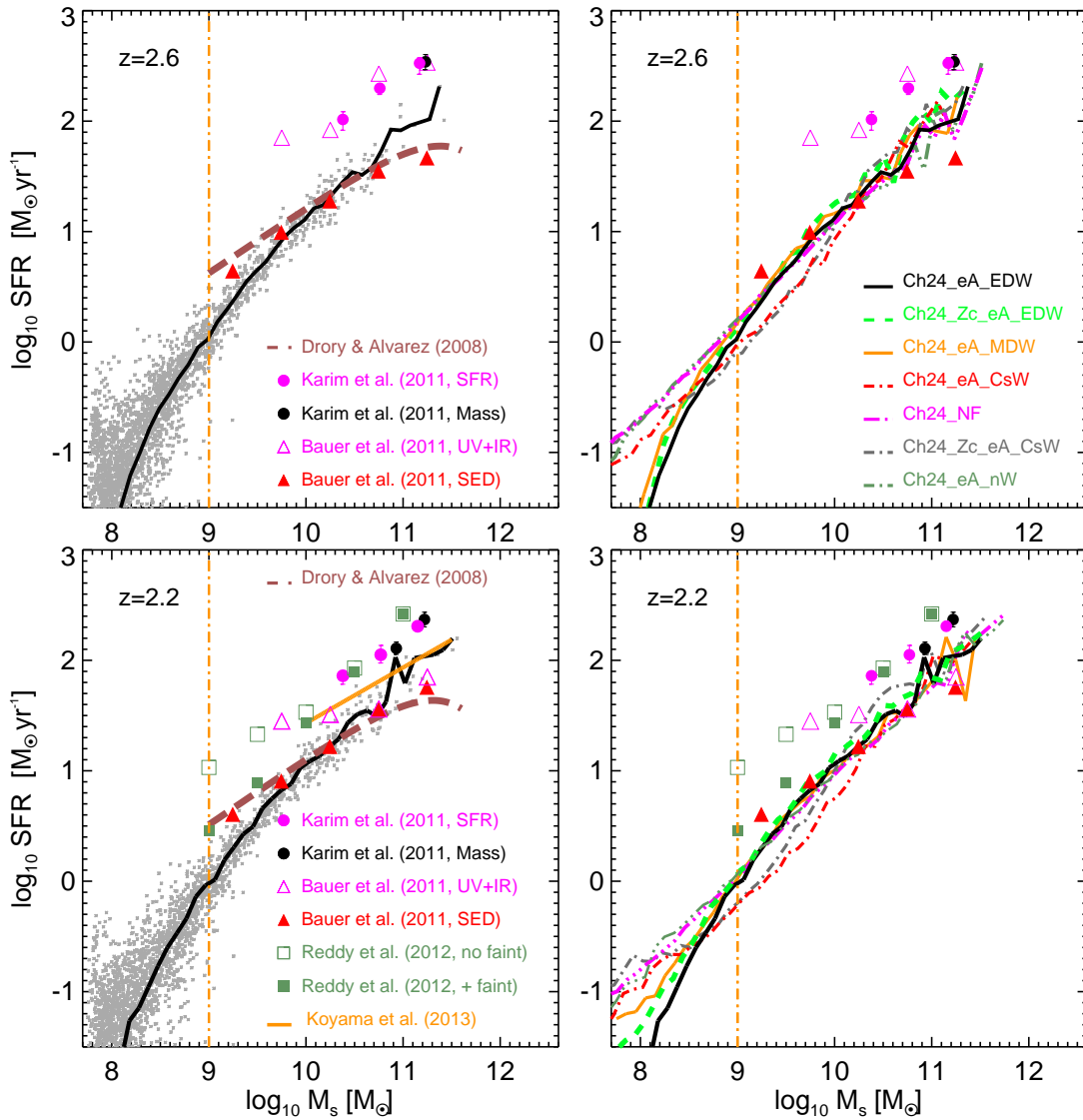


Figure 3. Left panels: scatter plot of the SFR– M_* relation for our fiducial run *Ch24_eA_EDW* (grey points) at redshifts $z \sim 2.2$ and 2.6 . In each panel, the black solid line is the median line through the points of the scatter plot. Overplotted are the observed galaxy SFR(M_*) relations from Drory & Alvarez (2008, mass selected sample - brown dashed line), Karim et al. (2011, SFR-selected/mass-selected sample - magenta/black circles with error bars), Bauer et al. (2011, mass-selected sample/SFRs that are obtained from SED fitting - red triangles), Bauer et al. (2011, $24 \mu\text{m}$ selected sample/SFRs that are obtained from UV+IR luminosities - magenta open triangles), Reddy et al. (2012, Lyman-break selected sample - dark green open squares are not corrected for incompleteness, dark green filled squares are the corrected results) and Koyama et al. (2013, $H\alpha$ -selected sample - orange solid line). Right panels: median lines of the SFR– M_* scatter plots for all the runs of Table 2. In these panels we do not present the analytic expressions of the observed relations for the sake of clarity.

and *Ch24_eA_EDW* models are consistent with the configurations that have no winds. This means that the effect of our variable wind models do not change the slope of the SFR– M_* relation. The only small difference between our runs is found for objects with $\log_{10}(M_*/M_\odot) \leq 8.5$, where there are no observations to constrain the results and feedback is not well resolved. This is in agreement with Davé (2008) and Dutton et al. (2010)². For this work we use a set of physically plausible cases that can produce realistic star

formation rate and stellar mass functions in our simulations (Tescari et al. 2014; Katsianis et al. 2015). In addition, by comparing the *Ch24_Zc_eA_CsW* and *Ch24_eA_CsW* we see that metal cooling does not significantly change the simulated SFR– M_* relation. This is due to the fact that when metal cooling is included gas can cool more efficiently. As a result the SFR increases and, correspondingly, the stellar mass increases moving galaxies along the SFR– M_* relation without affecting it considerably.

The scatter plot of the simulated SFR– M_* relation for our fiducial model at $z \sim 2.6$ (top left panel of Figure 3) is con-

²However, extreme feedback recipes can shape the SFR– M_* relation (Haas et al. 2013).

sistent with the results of the mass selected samples of Drory & Alvarez (2008) and Bauer et al. (2011). The open magenta triangles show the median SFR that relied on adding IR and UV luminosities (SFR_{IR+UV}) for the sample of galaxies of Bauer et al. (2011), which were detected only at $24\ \mu\text{m}$. The authors state that, at $z > 2.5$, the SFR_{IR+UV} is greater than the SFR obtained from SED and UV light by an average factor of 5. The full mass selected sample of Bauer et al. (2011) with dust correction laws that rely on SED fitting is almost 0.7 dex lower and in excellent agreement with numerical results (filled red triangles). This comparison points out how selection and dust correction methods can affect the relation reported by observers at $z \sim 2.6$. Bauer et al. (2011) note that the best way to robustly determine the SFR and the amount of dust extinction for each galaxy is to calculate the ultraviolet slope SED-fitting. We find indeed that, at this redshift, numerical results agree quite well with SFRs from SED-fitting and are in tension with SFRs from UV+IR conversions. Our simulations do not agree with the results of Karim et al. (2011), shown by the magenta filled circles (SFR selected sample) and black filled circles (mass selected sample), who used radio luminosities to obtain the intrinsic SFRs. It is noted that the SFRs obtained from radio luminosities are overestimated and in tension with other SFR indicators (e.g. Speagle et al. 2014). Simulations and SED observations suggest that star formation rates at a fixed stellar mass are overestimated by a factor of ~ 6 when radio luminosity-SFR conversions are used at this high redshift. For redshift $z = 2.6$, the *Ch24_eA-CsW* and *Ch24_Zc_eA-CsW* runs underpredict the SFR at a fixed M_\star for objects with stellar masses $\log_{10}(M_\star/M_\odot) \leq 10.2$. The rest of the configurations are consistent with each other and with the mass selected observations of Bauer et al. (2011) (top right panel of Figure 3). By comparing the *Ch24_Zc_eA_EDW* and *Ch24_eA_EDW* we see that metal cooling does not affect the simulated SFR- M_\star relation when energy driven winds are used. This is true for all redshifts considered in this work.

The simulated SFR- M_\star relation for $z \sim 2.2$ (bottom left panel of Figure 3) is consistent with the mass selected samples of Drory & Alvarez (2008) and Bauer et al. (2011). The results of Bauer et al. (2011) that were obtained using two different dust correction methods (open magenta triangles and red filled triangles) agree better at $z < 2.25$. In the bottom left panel of figure 3 we also present the observations of Reddy et al. (2012). We emphasize the comparison between the biased and unbiased results of Reddy et al. (2012) who investigated a set of galaxies at redshifts $1.5 < z < 2.6$. The authors quantified the effects of the non detection of faint objects in their flux limited selection. We see that the effect of the Malmquist bias (preferential selection of the most luminous-SFR galaxies at a fixed stellar mass) is important for low mass galaxies, and that the slope of the biased SFR- M_\star relation is therefore artificially shallow. The correction makes the slope steeper with an exponent close to unity, in accordance with cosmological simulations. Reddy et al. (2012) used combinations of IR and UV

luminosities to obtain the intrinsic SFRs and dust corrections at $z \sim 2.2$, and thus possibly overestimated the normalization of the SFR- M_\star relation with respect to SED observations and simulations. The H α selected sample of Koyama et al. (2013) seems to produce a relation with a higher normalization and this maybe is due to the fact that it preferably samples high star forming galaxies. Radio SFRs are almost a factor of ~ 4 larger than other estimates at $z \sim 2.2$. For redshift $z = 2.2$, the simulations with constant energy driven winds underpredict the SFR at a fixed mass for objects with $\log_{10}(M_\star/M_\odot) \leq 10.3$ (bottom right panel of Figure 3). However, the simulation with metal cooling and constant energy driven winds slightly overpredicts the SFR at fixed stellar mass for objects with $\log_{10}(M_\star/M_\odot) \geq 10.5$.

The SFR- M_\star relation for our reference model at $z \sim 2.0$ (top left panel of Figure 4) is consistent with the mass selected samples of Kajisawa et al. (2010, SED) and Bauer et al. (2011). In contrast, the results from the SFR selected sample of Daddi et al. (2007) and the mass selected sample of Kajisawa et al. (2010, UV+IR) imply a significantly higher normalization. Bauer et al. (2011) state that they find a flattened relation relative to Daddi et al. (2007). According to Bauer et al. (2011) this is either due to the fact that they are using a mass-complete sample instead of just star-forming galaxies, or the overestimation of the dust correction applied by Daddi et al. (2007) who used a combination of IR and UV luminosities instead of SED fitting. Daddi et al. (2007) considered only blue, star-forming galaxies and excluded quiescent objects from their analysis (using a magnitude cut) so their derived SFR- M_\star relation can be artificially higher at fixed stellar mass due to this reason. Furthermore, Hayward et al. (2014) note that the overestimation of SFRs from IR luminosities may have played an important role in the observed SFR- M_\star relations of Daddi et al. (2007) and suggest that the methodology used by the authors may have overestimated the SFRs at a fixed stellar mass. We see that the SFR selected results of Daddi et al. (2007, red triple dot-dashed line - IR+UV) and the mass selected sample of Kajisawa et al. (2010, dark green symbols - UV+IR) are in excellent agreement. This points to the direction that the SFR selection of Daddi et al. (2007) did not considerably affect the SFR- M_\star relation and the methodology for dust corrections and determinations of intrinsic SFRs is mostly responsible for the tension with the results of Kajisawa et al. (2010, blue symbols-UV $_{SED}$) and Bauer et al. (2011). Kajisawa et al. (2010) state that at $z \sim 2$ the ratio of SFR_{UV+IR} and $SFR_{UV_{SED}}$ is $\log(SFR_{IR+UV}/SFR_{UV_{SED}}) = 0.37$, for the same sample of galaxies. We also see from Figure 4 that the difference between the two methods for the determination of the intrinsic SFRs at a fixed stellar mass is ~ 0.75 dex for objects with $> 10^{10.5} M_\odot$. Simulations confirm again that at $z \sim 2$ object by object determinations of the amount of dust extinction from multiwavelength SED-fitting are more robust, while the use of IR light overpredicts the SFRs. For redshift $z = 2.0$, the simulations with constant energy driven winds underpredict the SFR at a fixed mass for objects with

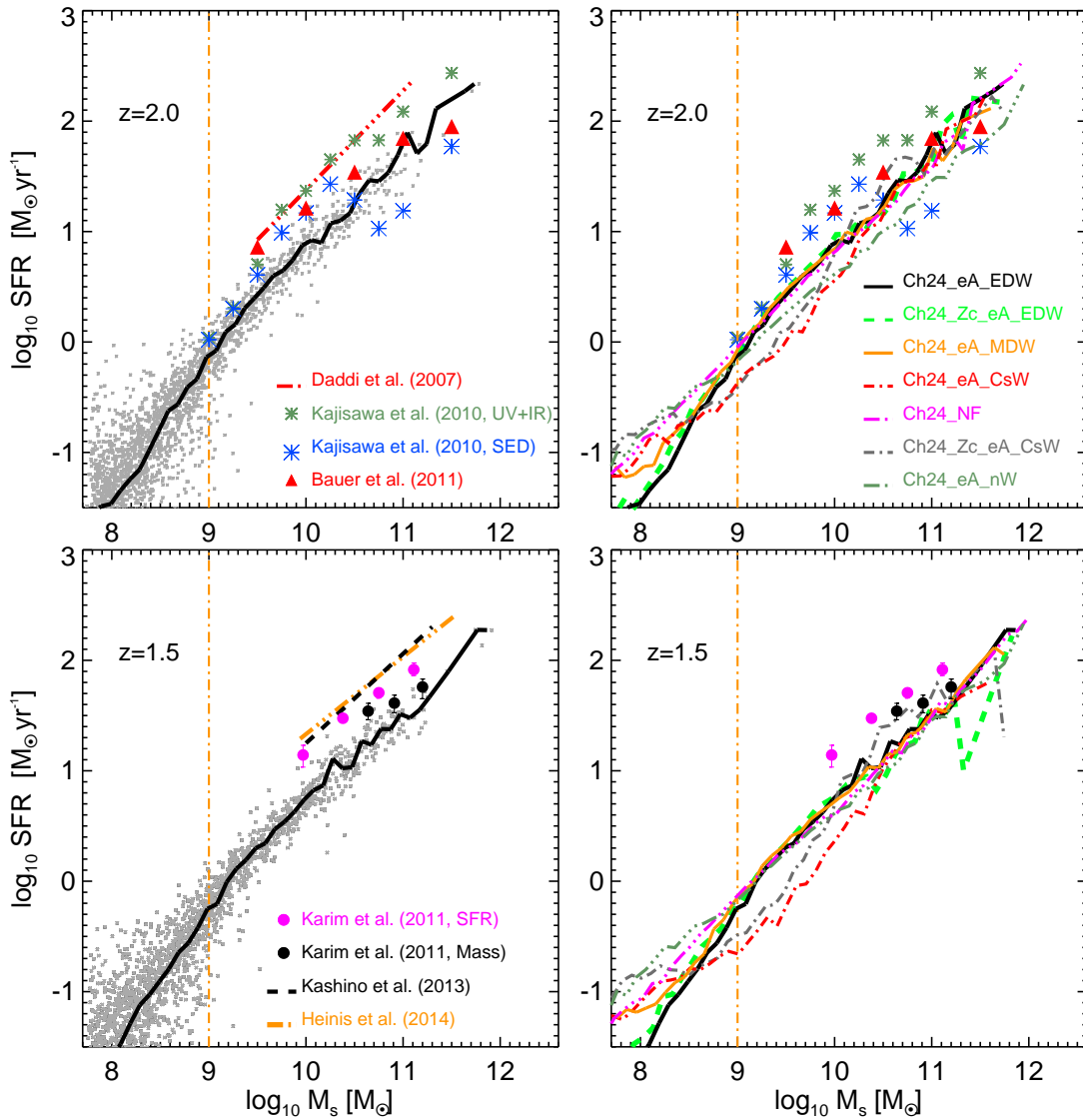


Figure 4. Left panels: scatter plot of the SFR– M_\star relation for our fiducial run *Ch24_eA_EDW* (grey points) at redshifts $z \sim 1.5$ and 2.0 . In each panel, the black solid line is the median line through the scatter plot. Overplotted are the observed galaxy SFR(M_\star) relations from Daddi et al. (2007, SFR selected sample - red triple dot-dashed line), Kajisawa et al. (2010, mass-selected sample, SED/UV+IR - blue stars/green stars), Karim et al. (2011, SFR-selected/mass-selected sample - magenta/black circles), Bauer et al. (2011, mass-selected sample - red triangles), Kashino et al. (2013, Lyman-break selected sample - black dashed line) and Heinis et al. (2014, Lyman-break selected sample - orange triple dot-dashed line). Right panels: median lines of the star SFR– M_\star scatter plots for all the runs of Table 2. In these panels we do not present the analytic expressions of the observed SFR– M_\star relations for the sake of clarity.

$\log_{10}(M_\star/M_\odot) \leq 10$ (top right panel of Figure 4). The simulation with metal cooling and constant energy driven winds overpredicts the SFR at fixed stellar mass for objects with $\log_{10}(M_\star/M_\odot) \geq 10$.

The simulated SFR– M_\star relation for the *Ch24_eA_EDW* at $z \sim 1.5$ (bottom left panel of Figure 4) is steeper with lower normalization than the results of Heinis et al. (2014). It seems that the normalization of the SFR– M_\star relation obtained by their sample is higher due to their Lyman-break selection and/or the methodology used to recover the intrinsic properties of galaxies. We see that the results from Lyman-break and star forming selected galaxies are in ex-

cellent agreement (Kashino et al. 2013; Heinis et al. 2014) and this points to the direction that they probably represent a similar population. The agreement of the simulations with the radio SFRs of Karim et al. (2011) is improved (especially for the mass selected sample). In general, the tension between numerical results and SFRs from radio luminosities decreases with redshift. The simulation with constant energy driven winds underpredicts the SFRs of all the objects. The star formation rate at a fixed mass is 3 times lower than in the other runs.

The scatter plot of the simulated SFR– M_\star relation for our reference model at $z \sim 1.15$ (top left panel of Figure 5) is

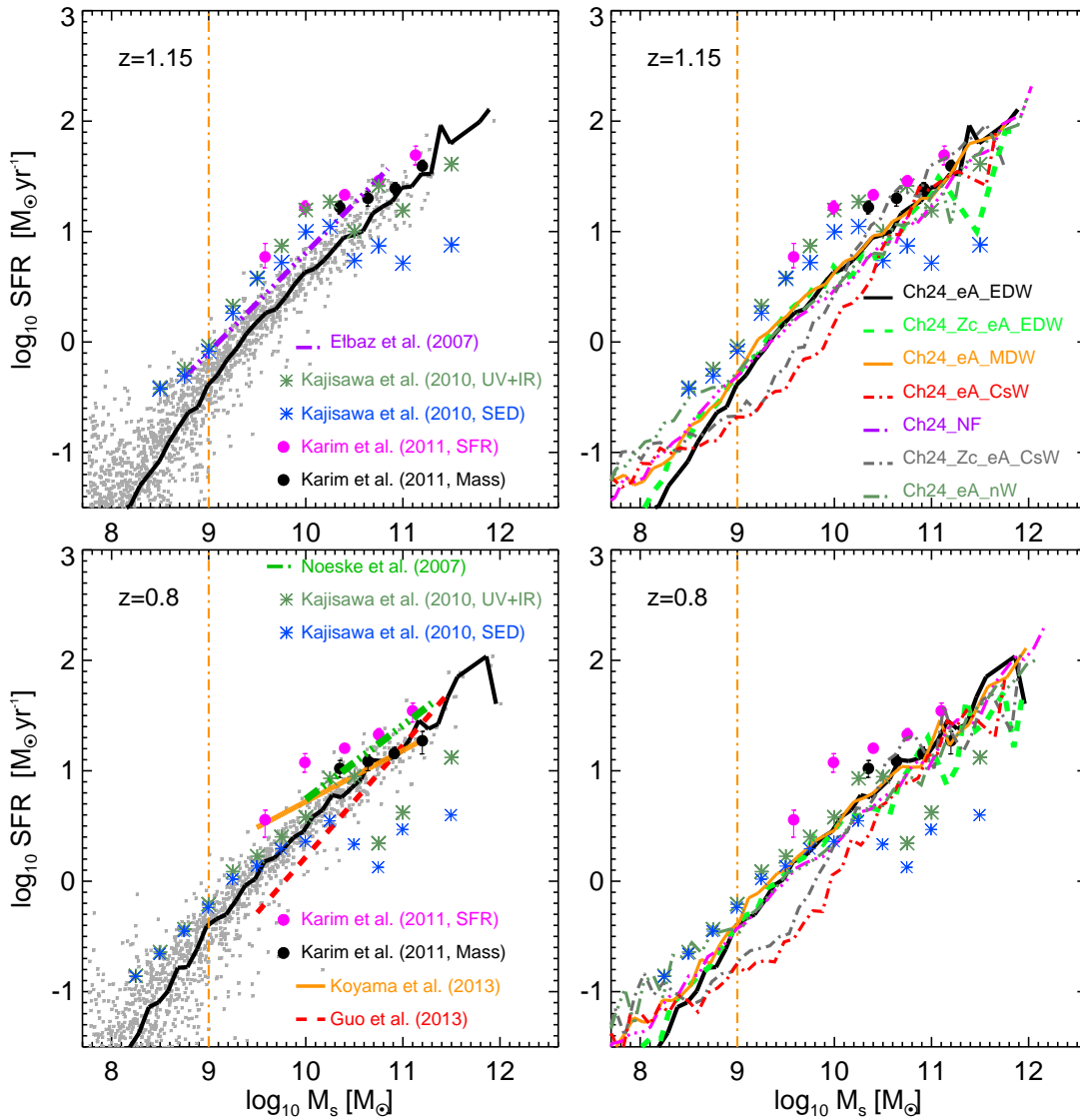


Figure 5. Left panels: scatter plot of the SFR- M_{\star} relation for our fiducial run *Ch24_eA_EDW* (grey points) at redshifts $z \sim 0.8$ and 1.15 . In each panel, the black solid line is the median line through the scatter plot. Overplotted are the observed galaxy SFR(M_{\star}) relations from Elbaz et al. (2007, SFR selected sample - magenta triple dot-dashed line), Noeske et al. (2007, SFR selected sample - green triple dot-dashed line), Kajisawa et al. (2010, mass-selected sample - SED/blue stars, IR+UV/dark green stars), Karim et al. (2011, SFR-selected/mass-selected sample - magenta/black circles), Guo et al. (2013, SFR selected sample - red dashed line) and Koyama et al. (2013, Ha-selected sample - orange solid line). Right panels: median lines of the SFR- M_{\star} scatter plots for all the runs of Table 2. In these panels we do not present the analytic expressions of the observed SFR- M_{\star} relations for the sake of clarity.

consistent with the results of the SFR selected samples of Elbaz et al. (2007), Kajisawa et al. (2010, for $M_{\star} \leq 10^{10.5} \text{M}_{\odot}$) and Karim et al. (2011). We see that the SFR selected relation reported by Elbaz et al. (2007) has slightly higher normalization and leads to larger values of star formation rates at a fixed mass for high mass objects. However, we see that the tension between the observed relations is much less and all agree well with numerical results. The difference between Kajisawa et al. (2010, dark green symbols-UV+IR) and Kajisawa et al. (2010, blue symbols-UV_{SED}) is much smaller than that found at higher redshifts. The authors state that $\log(\text{SFR}_{\text{IR+UV}}/\text{SFR}_{\text{UV}_{\text{SED}}})$ is ~ 0.25 and ~ 0.19 for $z \sim 1.25$ and $z \sim 0.75$, respectively. The difference between

the two methods to recover the intrinsic SFR at a fixed stellar mass for objects with $M_{\star} > 10^{10.5} \text{M}_{\odot}$ is ~ 0.35 dex and ~ 0.25 dex for $z \sim 1.25$ and $z \sim 0.75$, respectively (considerably lower than the 0.75 dex found at $z \sim 2.0$). The turn over of the relation found in the mass selected sample of Kajisawa et al. (2010) is most likely due to the fact that their mass selection is able to include massive quiescent galaxies (Drory & Alvarez 2008). Simulations (including ANUGS, Illustris and EAGLE) are unable to produce this behaviour. Once again, we see that the run with constant energy driven winds (*Ch24_eA_CsW*) underpredicts the SFR at a fixed mass (top right panel of Figure 5). The simulation with constant energy driven winds and metal cooling underpredicts the SFR

at a fixed stellar mass for $\log_{10}(M_{\star}/M_{\odot}) \leq 10.4$. On the contrary, for objects with $\log_{10}(M_{\star}/M_{\odot}) \geq 10.5$ the SFR is over-predicted. The other configurations are consistent with each other.

The simulated SFR– M_{\star} relation for our fiducial model at $z \sim 0.8$ (bottom left panel of Figure 5) is consistent with the SFR selected results of Noeske et al. (2007), the mass selected samples of Karim et al. (2011), the H α selected sample of Koyama et al. (2013) and the SFR selected sample of Guo et al. (2013). We see that the updated relation given by Guo et al. (2013) is steeper than the one given by Noeske et al. (2007). Guo et al. (2013) stressed that their results are significantly steeper than the results of Noeske et al. (2007) and sample selection is critical for determining the slope of the relation. If the authors fit only their relation to the 24 μm detected galaxies, they would get a much shallower slope in perfect agreement with Noeske et al. (2007). The authors note that the slope of the relation is largely determined by the detection of low-mass galaxies, which are crucial for the determination of the intrinsic slope (with an exponential slope close to unity). This result is consistent with Reddy et al. (2012) and cosmological simulations. As for the higher redshifts considered in this work, we find that simulations with constant energy driven winds underpredict the SFR at a fixed mass for objects with stellar masses lower than $\sim 10^{10.3} M_{\odot}$ (bottom right panel of Figure 5).

In conclusion, we find that simulations favor observations that rely on SED fitting for the determination of the intrinsic SFRs and dust corrections at $z > 1.5$. On the contrary, the combination of UV and IR luminosities overpredicts the star formation at a fixed stellar mass by almost a factor of 5. This finding confirms the results of Katsianis et al. (2015). For $z < 1.5$ simulations suggest that SFRs of high mass objects ($\log_{10}(M_{\star}/M_{\odot}) > 10.6$) that rely solely on UV luminosities are underpredicted. This is likely due to the fact that the dusty environment of high mass low redshift galaxies does not allow UV light to escape the galaxy and the SFR_{UV} ends up being underestimated. Kajisawa et al. (2010) also suggest that, if a galaxy has star-forming regions from which one can detect no UV light at all due to the heavy dust obscuration (this case occurs more frequently for low redshift galaxies with large masses), only UV light from relatively less-obscured regions contributes to the observed SED, and this results in the underestimation of the dust extinction. Furthermore, we see that sample selection can affect the results for the observed SFR– M_{\star} relation. The ratio of $\log(SFR_{Lyman,H\alpha,blue\ Selection}/SFR_{Mass\ Selection})$ at a fixed mass is ~ 0.1 dex to ~ 0.6 dex. The tension increases with mass and redshift. In general, numerical results from different groups are in better agreement with mass selected observations. The large tension with the normalizations and exponents of SFR– M_{\star} relations from Lyman-break, SFR and H α selected samples at all redshifts suggests that Lyman-break, SFR and H α selections could be biased and possibly do not take into account a significant number of objects. Cosmological simulations predict steeper slopes than observations,

with an exponent close to unity almost at all redshifts. Recent relations that take into account faint objects are significantly steeper than those found by past authors and this is in agreement with the results of Reddy et al. (2012), Guo et al. (2013) and the predictions from cosmological simulations. We note that our numerical results are in good agreement with the mass-selected observations of Kajisawa et al. (2010) even below the confidence limit of $10^9 M_{\odot}$. Lastly, we note that the uncertainty of the observed SFR– M_{\star} relation has possibly misguided numerical methods. We describe this in detail in appendix A. Simulations implemented with variable energy driven and momentum driven winds give the same results and are able to reproduce the observed relations, while models with constant winds fail to produce realistic results at low redshift.

5 Discussion and conclusions

In the previous sections we have investigated the evolution of the SFR– M_{\star} relation for galaxies at $z \sim 1 - 4$ using cosmological hydrodynamic simulations and a compilation of observed relations from various groups. In particular, we demonstrated that observational studies report a range of SFR– M_{\star} relations at high redshifts. The reason for the lack of consensus is related to the fact that different groups adopt different methods of selection and calculation of the intrinsic properties of galaxies. Overall, numerical results suggest that studies which use SED fitting to estimate the intrinsic SFRs, dust corrections and stellar masses for the observed objects produce more reliable SFR– M_{\star} relations. The tension between different groups becomes smaller at lower redshifts, where observations are more complete. This is due to the fact that various biases related to sample selection and limits of instrumentation become less severe.

A comparison between different simulations at $z \sim 1 - 4$ suggests that the assumed parameters for the AGN and variable winds feedback implementations do not affect the simulated SFR– M_{\star} relation within the range of models considered. While more extreme models can produce different SFR– M_{\star} relations (Haas et al. 2013), the models in this paper were chosen to reproduce the observed SFRF and GSMF at redshifts $z \sim 1 - 7$ (Tescari et al. 2014; Katsianis et al. 2015). We find that the scatter of the SFR– M_{\star} relation is ~ 0.2 dex at all redshifts, which is in agreement with estimates from recent observations (Whitaker et al. 2012; Speagle et al. 2014).

In the previous sections we demonstrated that the SFR– M_{\star} relations obtained from Lyman-break selected and SFR selected galaxies have significantly higher normalizations, when compared with stellar mass based selection and cosmological hydrodynamic simulations from various groups. This is due to the fact that these samples are biased to include the most luminous-star forming objects and possibly miss a large population of low SFR galaxies. This tends to increase the observed mean SFR at a fixed mass. In addition, due to incompleteness at the low mass end of the distri-

bution, the average/median star formation rates are overestimated for low mass objects (Malmquist bias, Reddy et al. 2012). This makes the observed relations artificially shallow in SFR selected samples and our simulations suggest that the intrinsic relations are steeper. In appendix A we demonstrate how old possibly biased past observations could have misguided simulations in the past.

Acknowledgments

The authors would like to thank Amanda Bauer, Naveen Reddy, Masaru Kajisawa, and Yusei Koyama for insightful discussions and for kindly sharing their observational results with us. In addition, we would like to thank Martin Sparre and Michelle Furlong for sharing their numerical results. We would also like to thank Volker Springel for making available to us the non-public version of the GADGET-3 code. This research was conducted by the Australian Research Council Centre of Excellence for All-sky Astrophysics (CAASTRO), through project number CE110001020. This work was supported by the NCI National Facility at the ANU.

REFERENCES

- Barai, P., Viel, M., Borgani, S., Tescari, E., Tornatore, L., Dolag, K., Killedar, M., Monaco, P., D’Odorico, V., & Cristiani, S. 2013, *MNRAS*, 430, 3213
- Bauer, A. E., Conselice, C. J., Pérez-González, P. G., Grützbauch, R., Bluck, A. F. L., Buitrago, F., & Mortlock, A. 2011, *MNRAS*, 417, 289
- Bauer, A. E., Hopkins, A. M., Gunawardhana, M., et al. 2013, *MNRAS*, 434, 209
- Behroozi, P. S., Wechsler, R. H., & Conroy, C. 2013, *ApJ*, 770, 57
- Boquien, M., Buat, V., & Perret, V. 2014, *A&A*, 571, A72
- Bouwens, R. J., Illingworth, G. D., Oesch, P. A., Franx, M., Labbé, I., Trenti, M., van Dokkum, P., Carollo, C. M., González, V., Smit, R., & Magee, D. 2012, *ApJ*, 754, 83
- Brinchmann, J. & Ellis, R. S. 2000, *ApJ*, 536, L77
- Broadhurst, T. J., Ellis, R. S., & Glazebrook, K. 1992, *Nat*, 355, 55
- Bruzual, G. & Charlot, S. 2003, *MNRAS*, 344, 1000
- Chabrier, G. 2003, *PASP*, 115, 763
- Crain, R. A., Schaye, J., Bower, R. G., Furlong, M., Schaller, M., Theuns, T., Dalla Vecchia, C., Frenk, C. S., McCarthy, I. G., Helly, J. C., Jenkins, A., Rosas-Guevara, Y. M., White, S. D. M., & Trayford, J. W. 2015, *MNRAS*, 450, 1937
- Daddi, E., Dickinson, M., Morrison, G., Chary, R., Cimatti, A., Elbaz, D., Frayer, D., Renzini, A., Pope, A., Alexander, D. M., Bauer, F. E., Giavalisco, M., Huynh, M., Kurk, J., & Mignoli, M. 2007, *ApJ*, 670, 156
- Davé, R. 2008, *MNRAS*, 385, 147
- Dayal, P. & Ferrara, A. 2012, *MNRAS*, 421, 2568
- de Barros, S., Schaerer, D., & Stark, D. P. 2014, *A&A*, 563, A81
- De Los Reyes, M., Lee, J. C., Ly, C., Salim, S., Momcheva, I. G., Feddersen, J., Dale, D. A., Ouchi, M., Ono, Y., & Finn, R. 2014, in *American Astronomical Society Meeting Abstracts*, Vol. 223, American Astronomical Society Meeting Abstracts 223, 227.02
- Drory, N. & Alvarez, M. 2008, *ApJ*, 680, 41
- Drory, N., Salvato, M., Gabasch, A., Bender, R., Hopp, U., Feulner, G., & Pannella, M. 2005, *ApJ*, 619, L131
- Dutton, A. A., van den Bosch, F. C., & Dekel, A. 2010, *MNRAS*, 405, 1690
- Elbaz, D., Daddi, E., Le Borgne, D., Dickinson, M., Alexander, D. M., Chary, R.-R., Starck, J.-L., Brandt, W. N., Kitzbichler, M., MacDonald, E., Nonino, M., Popesso, P., Stern, D., & Vanzella, E. 2007, *A&A*, 468, 33
- Ferland, G. J., Porter, R. L., van Hoof, P. A. M., Williams, R. J. R., Abel, N. P., Lykins, M. L., Shaw, G., Henney, W. J., & Stancil, P. C. 2013, arxiv:1302.4448
- Finlator, K., Davé, R., & Özel, F. 2011, *ApJ*, 743, 169
- Furlong, M., Bower, R. G., Theuns, T., Schaye, J., Crain, R. A., Schaller, M., Dalla Vecchia, C., Frenk, C. S., McCarthy, I. G., Helly, J., Jenkins, A., & Rosas-Guevara, Y. M. 2015, *MNRAS*, 450, 4486
- Genel, S., Vogelsberger, M., Springel, V., Sijacki, D., Nelson, D., Snyder, G., Rodriguez-Gomez, V., Torrey, P., & Hernquist, L. 2014, *MNRAS*, 445, 175
- Gilbank, D. G., Bower, R. G., Glazebrook, K., Balogh, M. L., Baldry, I. K., Davies, G. T., Hau, G. K. T., Li, I. H., McCarthy, P., & Sawicki, M. 2011, *MNRAS*, 414, 304
- Guo, K., Zheng, X. Z., & Fu, H. 2013, *ApJ*, 778, 23
- Haardt, F. & Madau, P. 2001, in *Clusters of Galaxies and the High Redshift Universe Observed in X-rays*, ed. D. M. Neumann & J. T. V. Tran
- Haas, M. R., Schaye, J., Booth, C. M., Dalla Vecchia, C., Springel, V., Theuns, T., & Wiersma, R. P. C. 2013, *MNRAS*, 435, 2955
- Hayward, C. C., Lanz, L., Ashby, M. L. N., Fazio, G., Hernquist, L., Martínez-Galarza, J. R., Noeske, K., Smith, H. A., Wuyts, S., & Zezas, A. 2014, *MNRAS*, 445, 1598
- Heinis, S., Buat, V., Béthermin, M., Bock, J., et al. 2014, *MNRAS*, 437, 1268
- Kajisawa, M., Ichikawa, T., Yamada, T., Uchimoto, Y. K., Yoshikawa, T., Akiyama, M., & Onodera, M. 2010, *ApJ*, 723, 129
- Kannan, R., Stinson, G. S., Macciò, A. V., Brook, C., Weinmann, S. M., Wadsley, J., & Couchman, H. M. P. 2014, *MNRAS*, 437, 3529
- Karim, A., Schinnerer, E., Martínez-Sansigre, A., & others. 2011, *ApJ*, 730, 61
- Kashino, D., Silverman, J. D., Rodighiero, G., et al. 2013, *ApJ*, 777, L8
- Katsianis, A., Tescari, E., & Wyithe, J. S. B. 2015, *MNRAS*, 448, 3001
- Kennicutt, Jr., R. C. 1998, *ARA&A*, 36, 189
- Koyama, Y., Smail, I., Kurk, J., Geach, J. E., Sobral, D.,

- Kodama, T., Nakata, F., Swinbank, A. M., Best, P. N., Hayashi, M., & Tadaki, K.-i. 2013, *MNRAS*, 434, 423
- Kroupa, P. 2001, *MNRAS*, 322, 231
- Magdis, G. E., Rigopoulou, D., Huang, J.-S., & Fazio, G. G. 2010, *MNRAS*, 401, 1521
- Meurer, G. R., Heckman, T. M., & Calzetti, D. 1999, *ApJ*, 521, 64
- Murante, G., Monaco, P., Borgani, S., Tornatore, L., Dolag, K., & Goz, D. 2015, *MNRAS*, 447, 178
- Noeske, K. G. et al. 2007, *ApJ*, 660, L43
- Puchwein, E. & Springel, V. 2013, *MNRAS*, 428, 2966
- Reddy, N. A., Pettini, M., Steidel, C. C., Shapley, A. E., Erb, D. K., & Law, D. R. 2012, *ApJ*, 754, 25
- Salmon, B., Papovich, C., Finkelstein, S. L., Tilvi, V., Finlator, K., Behroozi, P., Dahlen, T., Davé, R., Dekel, A., Dickinson, M., Ferguson, H. C., Giavalisco, M., Long, J., Lu, Y., Mobasher, B., Reddy, N., Somerville, R. S., & Wechsler, R. H. 2015, *ApJ*, 799, 183
- Salpeter, E. E. 1955, *ApJ*, 121, 161
- Schaye, J., Crain, R. A., Bower, R. G., Furlong, M., et al. 2015, *MNRAS*, 446, 521
- Sobral, D., Smail, I., Best, P. N., Geach, J. E., Matsuda, Y., Stott, J. P., Cirasuolo, M., & Kurk, J. 2013, *MNRAS*, 428, 1128
- Sparre, M., Hayward, C. C., Springel, V., Vogelsberger, M., Genel, S., Torrey, P., Nelson, D., Sijacki, D., & Hernquist, L. 2015, *MNRAS*, 447, 3548
- Speagle, J. S., Steinhardt, C. L., Capak, P. L., & Silverman, J. D. 2014, arXiv:1405.2041
- Springel, V. 2005, *MNRAS*, 364, 1105
- Springel, V. & Hernquist, L. 2003, *MNRAS*, 339, 289
- Tescari, E., Katsianis, A., Wyithe, J. S. B., Dolag, K., Tornatore, L., Barai, P., Viel, M., & Borgani, S. 2014, *MNRAS*, 438, 3490
- Tornatore, L., Borgani, S., Dolag, K., & Matteucci, F. 2007, *MNRAS*, 382, 1050
- Utomo, D., Kriek, M., Labbé, I., Conroy, C., & Fumagalli, M. 2014, *ApJ*, 783, L30
- Vogelsberger, M., Genel, S., Sijacki, D., Torrey, P., Springel, V., & Hernquist, L. 2013, *MNRAS*, 436, 3031
- Whitaker, K. E., van Dokkum, P. G., Brammer, G., & Franx, M. 2012, *ApJ*, 754, L29
- Wiersma, R. P. C., Schaye, J., & Smith, B. D. 2009, *MNRAS*, 393, 99

A Have past observed SFR– M_{\star} relations misguided simulations?

In this appendix we demonstrate how the uncertainty of dust correction laws and selection effects/biases have been affecting the comparison with cosmological simulations for the past decade. In figure A1 we show a compilation of median SFR– M_{\star} relations from cosmological hydrodynamic simulations and semi-analytic models alongside with observations from various groups.

Davé (2008) investigated the tension between observed and simulated results for the SFR– M_{\star} and extensively discussed how to address it. In general, the numerical results implied steeper relations with lower normalization than observations. The author considered various modifications of the theoretical picture of stellar mass assembly, but each was found to be in conflict with observations of high-redshift galaxies. In light of this tension, Davé (2008) suggested an evolving IMF to address the discrepancy. Is it possible though, that the observations used (e.g. Noeske et al. 2007; Daddi et al. 2007) to constrain the simulations contained biases or/and overestimated the SFR at fixed stellar mass? For redshift 0, we see that the numerical results of Davé (2008) are in excellent agreement with current state of art cosmological simulations of the Illustris and EAGLE projects, despite of the fact that the resolution is higher and box sizes are larger for the updated simulations. At redshift $z \sim 1$, the amplitude of the simulated relation presented by Davé (2008) is steeper than the observations of Noeske et al. (2007). However, in the previous sections we saw that the results of Noeske et al. (2007) were artificially shallower due to the fact that they were not taking into account low mass/SFR objects. The updated results from Guo et al. (2013) that take into account low SFR objects and $24\mu\text{m}$ undetected objects, are significantly steeper with a power law exponent close to unity. Once again, at $z \sim 1$ we see the perfect agreement between the numerical results of the Illustris and EAGLE projects and the simulated relation from Davé (2008). Moving to $z \sim 2$, Davé (2008) reported a significant tension, with an amplitude offset of $\sim 4 - 5$, with the results of Daddi et al. (2007). In the above sections we provided strong indications that the relation given by Daddi et al. (2007) has artificially high normalization and an artificially shallower slope, since the authors preferably selected star forming galaxies and relied on SFRs that were obtained from UV+IR luminosities (Bauer et al. 2011; Hayward et al. 2014). The numerical results of Davé (2008) are in good agreement with the simulated SFR– M_{\star} from the ANGUS, Illustris and EAGLE projects, and the mass selected observations that adopt SED fitting techniques to obtain dust corrections and SFRs. It seems that the tension between observed and simulated relations reported by Davé (2008) had its roots in the fact that past observations were overestimating the SFR at a fixed stellar mass due to methodology, sample selection effects and biases related to undetected faint objects.

Sparre et al. (2015) stated that there is good consistency between the simulated and observed (Behroozi et al. 2013) SFR– M_{\star} relations at $z \sim 0$ and $z \sim 4$. However, at intermediate redshifts there is a severe tension. We stress that while the results of Behroozi et al. (2013) are a compilation of observations, the authors did not account for the fact that these observations assumed completely different methods to produce SFR– M_{\star} relations. Different methods produce completely different results and for this reason they should not be compiled directly all together. The results of Behroozi et al. (2013) for redshifts $z \sim 1 - 2$ were mostly based on samples that preferably selected star forming galaxies and assumed IR+UV luminosities to obtain the intrinsic SFRs (Noeske et al. 2007; Daddi et al. 2007; Whitaker et al. 2012). Therefore, the compilation overpredicts the SFR at a fixed stellar mass for these redshifts, with respect to mass selected surveys that used detailed SED fitting. In Figure A1 we show that all models underpredict the SFR at a fixed stellar mass for $z \sim 1 - 2$, with respect to the compilation of observations in Behroozi et al. (2013). The comparison suggests that it is quite possible that the compilation did not take into account the faint objects at $z \sim 1 - 2$ and therefore suffers from the Malmquist

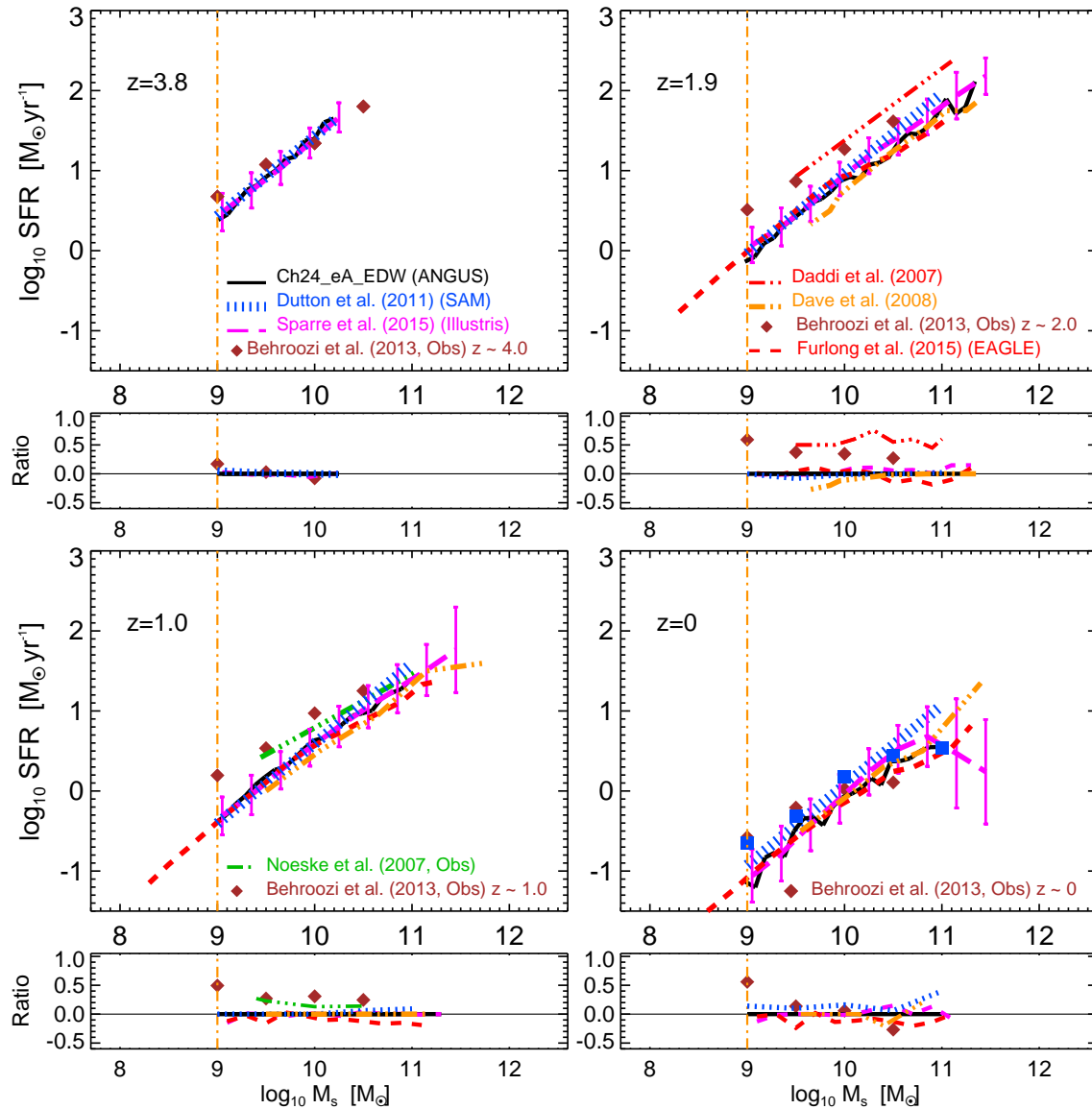


Figure A1. Median values of the SFR– M_* relations from different cosmological hydrodynamic simulations for $z \sim 4$ – 0 . The black line is our reference model (*Ch24_eA_EDW*). The dark green dotted line is the median fit of the scatter plot presented by Davé (2008). The blue dotted line is the median fit of the scatter plot presented by Dutton et al. (2010, SAM). The magenta dashed line is the median line of the scatter plot presented by Sparre et al. (2015, Illustris project). The red dashed line is the median line of the scatter plot presented by Furlong et al. (2015, EAGLE project). We cut our SFR(M_*) under our confidence mass limit of $10^9 M_\odot$ to make a meaningful comparison with the Illustris and EAGLE projects. There is an excellent agreement between the results from cosmological hydrodynamic simulations run by different groups. At each redshift, a panel showing ratios between the different simulations and observations with the *Ch24_eA_EDW* (black solid line) is included.

bias (the difference with the intrinsic relation suggested by simulations increases at lower masses). A correction to lower star formation rates would be expected, as in Reddy et al. (2012), in order to obtain an unbiased relation due to incompleteness. This would bring observations and simulations to better agreement.

In conclusion, the tension reported in the literature likely has its roots in the fact that the comparisons have been done using relations that overpredict the SFR at a fixed stellar mass due to selection biases and/or methodology. Cosmological simulations in the past decade indicate that the slope of the relation is steeper with a lower normalization. Of course, it is possible that this slope is the result of a poor representation of physical processes, which are im-

plemented in a similar way by simulators (ANGUS, EAGLE, Illustris). We demonstrated that the simulated SFR– M_* relations from various groups are in excellent agreement and largely independent of resolution and box size. Maybe further attention have to be given in subgrid physics. More work is needed to improve the numerical modeling of star formation, and in particular the description of the ISM.